MIT Open Access Articles

Cyclic martensitic transformations and damage evolution in shape memory zirconia: Single crystals vs polycrystals

Citation	Crystal, Isabel R., Lai, Alan and Schuh, Christopher A. 2020. "Cyclic martensitic transformations and damage evolution in shape memory zirconia: Single crystals vs polycrystals." Journal of the American Ceramic Society, 103 (8).
As Published	http://dx.doi.org/10.1111/jace.17117
Publisher	Wiley
Version	Author's final manuscript
Citable link	https://hdl.handle.net/1721.1/140941
Terms of Use	Creative Commons Attribution-Noncommercial-Share Alike
Detailed Terms	http://creativecommons.org/licenses/by-nc-sa/4.0/

MISS ISABEL R. CRYSTAL (Orcid ID : 0000-0003-0184-4881)

PROFESSOR CHRISTOPHER A. SCHUH (Orcid ID : 0000-0001-9856-2682)

Article type   : Article

Title: Cyclic martensitic transformations and damage evolution in shape memory zirconia:
single crystals vs. polycrystals

Authors:

Isabel R. Crystal[1], Alan Lai[1], & Christopher A. Schuh[*,1]

[1]*Department of Materials Science and Engineering, Massachusetts Institute of Technology, 77 Massachusetts Ave, Cambridge, MA 02139, United States*

[*]*Corresponding author. E-mail address: schuh@mit.edu (C.A. Schuh)*

Abstract

In zirconia-based shape memory ceramics (SMCs), cracking during the martensitic transformation can be avoided in structures that reduce the relative presence of grain boundaries where high levels of transformation mismatch stress develop. This approach has been well established in single crystals, but only for sample sizes below about 5 microns. In this paper, we extend the strategy of eliminating grain boundaries to bulk specimen scales by fabricating mm-scale single crystal SMCs via cold crucible induction melting. For 1.5 and 2.0 mol% Y_2O_3-ZrO_2, we study cyclic martensitic transformation of both single crystal and polycrystal structures.

Whereas single crystals have very repeatable transformation behavior in terms of hysteresis and strain amplitude, polycrystals degrade dramatically as they accumulate cracking damage with repeated cycling. As the polycrystal evolves from a pellet to granular packing of loose single crystals/grains, the energy dissipation converges with that of the single crystal structure, and the energy spent on cracking throughout that process is captured by calorimetry analysis. These results verify that grain boundaries play a key role in damage evolution during martensitic transformation, and microstructural control can extend the size-scale of viable single-crystal or oligocrystal SMCs from the micro- to the millimeter scale.

Keywords: shape memory, ceramics, zirconia, microstructure, single crystal, cracking

Introduction

The field of shape memory materials has come to include both metals and ceramics, with the latter of increasing interest due to their potential advantages of higher martensitic transformation temperatures and stresses, improved oxidation and wear resistance, and higher energy dissipation and work output as compared with shape memory alloys (SMAs). However, there are still shortcomings that need to be addressed before shape memory ceramics (SMCs) can be used more broadly as viable alternatives to SMAs. One of the most fundamental limitations of SMCs that undergo a martensitic transformation is that they are prone to transformation cracking. For example, ZrO_2 experiences large shape strains of ~16% and a volume expansion of ~4% during the tetragonal to monoclinic phase transformation, and is widely known to crack under these strains during processing (1–3).

There are a variety of strategies to avoid cracking in ZrO_2-based ceramics. Alloying with tetragonal- or cubic-stabilizing oxides like Y_2O_3 can suppress the martensitic transformation to temperatures below room temperature (as in partially or fully-stabilized tetragonal zirconia polycrystals, TZP), or even avoid the parent tetragonal phase entirely in favor of the cubic phase (2,4–7). This approach also underpins 'transformation toughening', whereby the transformation is suppressed during processing (sintering and cooling), but can still be accessed under high stresses such as near a crack, promoting crack closure (2,5,6). While stabilization is by far the

most common and widely adopted method of avoiding transformation cracking in ZrO_2, it is not suitable for SMCs, in which the transformation must be reversibly accessed in order to achieve shape memory properties. Any strategy that avoids the transformation entirely, such as sintering at low temperatures to attain a full density compact in the monoclinic phase without ever passing through the transformation temperature, would be similarly unsuitable for SMCs (1). Thus, methods of avoiding transformation cracking while undergoing the transformation are more specifically needed for SMCs.

At compositions where the martensitic transformation can be reversibly accessed, ZrO_2 ceramics exhibit the signatures of shape memory but are limited by eventual cracking (4,8–10). Reyes-Morel et al. (4) assessed the cyclic performance of a stress-driven superelastic transformation in polycrystalline CeO_2-ZrO_2 and observed diminishing hysteresis with each successive cycle until failure on the 5th cycle. This failure was attributed to intergranular fracture brought on by the mismatch stresses developed amongst the phases and grains. Lai et al. (11) observed that this intergranular cracking in CeO_2-ZrO_2 was reminiscent of that seen in metallic Cu-based shape memory alloys (12,13), where transformation strains cause cracking at grain boundaries but where cracking can be avoided by using specimens with relatively fewer grain boundaries and triple junctions (14–16). The same approach was applied to ZrO_2 by reducing the size scale of the specimen to achieve "oligocrystalline" micropillars and microparticles with few grain junctions and constraints (11,17). The decrease in size scale also correlates to an increase in the surface-area-to-volume ratio, thus resulting in more available free surface to facilitate stress relaxation. Such micropillars could recover significantly larger strains over 7% and could also be cycled over 50 times without fracture (11). In superelastic cycling experiments conducted on micron-sized single crystal particles of CeO_2-ZrO_2, fracture occurred in the range of 50 to 100 cycles, which is consistent with the micropillar study (18). In a related study, similar microparticles were shown to exhibit cyclic superelasticity over hundreds of cycles with a maximum of 502 cycles probed (19). Subsequent work on open cell foams (20) and granular packings (21,22) demonstrated extension of shape memory properties to larger length scales by assembly of those smaller particles into larger structures. Notably, the open cell foam structures studied by Zhao et al. (20) exhibited a thermally activated recoverable strain of 2% and stress induced transformation without fracture.

Among all the studies outlined above, we note that the cyclical performance of shape memory ceramics has yet to be assessed for bulk specimens beyond the scale of a few micrometers; the largest micropillar reported experimentally was at a scale of 2.5 µm diameter (23), while the struts of the foam in Ref. (20) were about 7.4 µm with grain sizes of 3.0 to 3.5 µm across, and the granular shape memory ceramic powders in Ref. (21) were < 3.0 µm in size. It is therefore an open question whether the reduction of grain boundary area can unlock desirable cyclic shape memory transformations at larger specimen scales. It is the purpose of this work to explore this issue in single crystal and polycrystal ZrO_2-based SMC compositions at the millimeter size scale. We explore thermal transformation cycles in such SMCs to reveal the role of grain boundaries on damage accumulation.

Experimental Materials

We selected yttria-doped ZrO_2 compositions for which the thermally triggered transformation is easily accessible, and can be characterized by four transformation temperatures: M_s and M_f, respectively correspond to martensite start and finish observed on cooling, while A_s and A_f denote austenite start and finish observed on heating. Here the term 'martensite' refers to the monoclinic phase and 'austenite' to tetragonal. The characteristic transformation temperatures decrease with yttria content, from ~1000 °C in undoped ZrO_2 to ~400 °C at about 2.0 mol% Y_2O_3 (23). We selected two compositions for detailed study, 1.5 mol% Y_2O_3-ZrO_2 and 2.0 mol% Y_2O_3-ZrO_2, which we prepared in both polycrystal and single crystal structures.

Differential scanning calorimetry (DSC, TGA/DSC 1, Mettler Toledo) was conducted on both polycrystal and single crystal specimens in air over the range 225 to 800 °C, with a heating and cooling rate of 15 °C/min to capture the critical transformations temperatures for each selected composition, as summarized in Table 1. In the subsequent sections, we detail the preparation of these samples.

A. Single Crystals

Because we are interested in bulk specimens with as few grain boundaries as possible, we elected to process specimens using a cold-crucible induction melter, or skull melter. This method

features extreme temperatures and controlled slow cooling and is amenable to the production of large ceramic single crystals; the method is commonly used to make single crystals of cubic zirconia (24–26). We applied this technique to our SMC compositions and had ingots of 1.5 mol% Y_2O_3-ZrO_2 and 2.0 mol% Y_2O_3-ZrO_2 prepared at SurfaceNet Gmbh (Rheine, Germany). The output of this process was approximately 250 mL of solidified ceramic, which appeared to comprise individual large grains with a long axis of preferential growth along the axis of the induction coil. We extracted our single crystal samples by mechanically harvesting large individual grains from the polycrystalline ingot. These grains were typically 3-4 mm in size, irregularly shaped, and partially translucent but not clear due to a multi-variant/multi-domain substructure as reported previously for solidification of similar compositions from a melt (27). The term 'single crystal' therefore most strictly pertains to the inferred structure of the parent (tetragonal) grain solidified at high temperatures, which transforms (incompletely) to a multi-domain monoclinic structure; for convenience we refer to the samples as 'single crystals' irrespective of their phase state. The extracted single crystal specimens were ground on two sides to create parallel faces (with an irregular perimeter shape) and a thickness of about 2.0-3.5 mm for testing, with no control for crystallographic orientation. A stereo microscope (Barska) equipped with a digital camera attachment (OptixCam summit series) was used for imaging the top surface of the single crystal sample **(Fig. 1a,d)**.

X-ray diffraction (XRD, D8, Bruker) was conducted with Cu k_α radiation at room temperature. 2D patterns were collected in Laue mode, and subsequently converted to 1D powder-like patterns with 2θ ranging from 22.5 to 42.5°, by integrating the Debye rings (**Fig. 1b,e** with 2D pattern inset). The phase content, which comprises the volume fraction of the monoclinic phase, V_m, and that of the tetragonal phase, $V_t = 1 - V_m$, was computed using the approach of Toraya et. al (28) that has been shown to have excellent correspondence to Rietveld refinement in the monoclinic-tetragonal zirconia system (29):

$$X_m = \frac{I(11\bar{1})_m + I(111)_m}{I(11\bar{1})_m + I(111)_m + I(101)_t} \tag{1a}$$

$$V_m = \frac{1.311\, X_m}{1 + 0.311\, X_m} \tag{1b}$$

where $I(111)_m$ and $I(11\overline{1})_m$ are the integrated intensities for the respective monoclinic peaks, I $(101)_t$ is the integrated intensity for the tetragonal 101 peak, and X_m is the integrated intensity ratio quantified by fitting the pattern to a pseudo Voigt profile using HighScore Plus software. At room temperature in the as-prepared condition, the 2.0 mol% Y_2O_3 single crystal was found to be 60% monoclinic while the 1.5 mol% Y_2O_3 single crystal was 69% monoclinic; the fine domain structure in the solidified structure could be responsible for preventing full martensitic transformation even when below the M_f temperature. The DSC curves in **Fig. 1c,f**, show clear endothermic peaks on heating through the critical austenite temperatures, where the specimen undergoes transformation from the monoclinic to tetragonal phase, and exothermic peaks on cooling as the specimen reverts back to the monoclinic phase. Note, within a batch or given composition of single crystals produced via cold-crucible induction melting, there is some variability with respect to the transformation temperatures and shape of the exothermic and endothermic peaks owing to the formation of different transformation correspondences or variants, which can explain the presence of double peaks as in **Fig 1c**. However, the 1.5 mol% Y_2O_3 composition consistently exhibits higher transformation temperatures relative to 2.0 mol% Y_2O_3 single crystals.

B. Polycrystals

Polycrystalline specimens were produced through a powder route by the Pechini method (30–32). Zirconium oxychloride octahydrate ($ZrOCl_2 \cdot 8H_2O$, Strem Chemicals) and yttrium nitrate hexahydrate ($Y(NO_3)_3 \cdot 6H_2O$, Strem Chemicals) solutions were combined according to the formula $xY_2O_3\text{-}(100\text{-}x)ZrO_2$ where x refers to the target dopant concentration and is selected to be 1.5 and 2.0 mol% Y_2O_3 to match the single crystal specimens above. The solution was homogenized by stirring under mild heat (275 °C), after which citric acid monohydrate was added as a chelating agent in a 4:1 molar ratio of citric acid to metal cation. After further homogenization, ethylene glycol was added as a polymerization agent in a 5:1 molar ratio of citric acid to ethylene glycol, and the solution was heated to gelatinization. The gel was dried at 150 °C into a crisp, dark orange compact, which was crushed and calcined in air at 600 °C for 2 h with a 5 °C/min ramp rate. The calcined product was ground into fine powder with a mortar and

pestle. The powder was then introduced into a 6.35 mm die and pressed at 200 MPa before sintering at 1500 °C for 10 h with a 10 °C/min ramp rate.

A scanning electron microscope (SEM, JSM-6610LV, JEOL) was used in low vacuum mode at 40 Pa to assess the grain size of the polycrystalline microstructures. The 1.5 mol% Y_2O_3 pellet had an average grain size of 1.0 μm as compared to the 2.0 mol% Y_2O_3 pellet which had a somewhat finer grain size of 0.8 μm (**Fig. 2a,d**). Powder x-ray diffraction (XRD, X'Pert Pro, PANalytical) with a heating stage (furnace, HTK1200N, Anton Paar) was conducted with Cu k_α radiation with 2θ ranging from 22.5 to 42.5° from room temperature to ~750 °C. According to the phase diagram proposed by Ruh et al. (33), the sintering temperature for the 2 mol% Y_2O_3 polycrystal sample falls within the tetragonal and cubic phase fields such that the cubic phase could be expected to form in small quantities. However, the slow cooling of the samples from the processing temperature ensured that any cubic phase that formed reverted to the tetragonal phase. A full XRD pattern collected at room temperature was examined and all peaks could be indexed with tetragonal or monoclinic reflections. By computing the monoclinic content V_m, using Eq. 1, for each measured temperature, a hysteresis curve can be constructed for each composition as shown in **Fig. 2b,e**. For both specimens, the monoclinic content is observed to gradually decrease on heating followed by a region of rapid decrease once A_s is reached until A_f, after which the monoclinic content reaches a stable minimum. On cooling, the monoclinic content begins to increase when M_s is reached until M_f, after which a stable maximum value is reached. The 1.5 mol% Y_2O_3 specimen shows a 87.6% change in monoclinic content (max. 94.0%, min. 6.5%) as compared to the 2.0 mol% Y_2O_3 pellet which only undergoes a change of 77.9% (max. 88.2%, min. 10.3%). DSC curves exhibited the expected transformation peaks on heating and cooling (**Fig. 2c,f**).

Cycling Behavior

Cyclic martensitic transformations were studied in a thermal mechanical analyzer (TMA, model 402 F3 Hyperion, Netzsch) in air using triangular thermal cycles over the range 200 to 900 °C at a rate 15 °C/min and under a negligible fixed load of 0.1 N. **Fig. 3** depicts a typical response curve for the 1.5 mol% Y_2O_3 polycrystal sample, which initiates with dilatation upon heating due to thermal expansion within the monoclinic phase. In the polycrystal sample, this region is

followed by a section of gradual shrinkage that initiates at ~380 °C, which could point to a small amount of transformation from the monoclinic to the tetragonal phase prior to reaching A_s. This observation is consistent with the slight decrease in measured monoclinic phase fraction with temperature in **Fig. 2b** prior to A_s. The measured slope of ~5.3×10^{-6} K^{-1} for the 1.5 mol% Y_2O_3 single crystal specimen of unknown crystallographic orientation is in line with reported values, which range from 1.4×10^{-6} K^{-1} to 8.0×10^{-6} K^{-1} for monoclinic ZrO_2 (34,35). Once the critical temperature, A_s, is reached, there is a large shrinkage strain associated with phase transformation to the tetragonal phase, which is complete at A_f. The slope on cooling is the tetragonal coefficient of thermal expansion, measured as 1.2×10^{-5} K^{-1} here, again in good agreement with reported values for pure ZrO_2 in the tetragonal phase, which range from 1.07×10^{-5} K^{-1} to 1.31×10^{-5} K^{-1} (34,35). Upon cooling to M_s, the specimen begins to dilate as the monoclinic phase evolves, completing at M_f.

The shape and details of the thermal cycling curve of **Fig. 3** evolve with the number of cycles, and in what follows we have therefore extracted several numerical quantities for analysis including (a) the residual strain after a full cycle, (b) the strain amplitude of the transformation, and (c) thermal hysteresis of the transformation; these alphabetic labels are shown in **Fig. 3**. Thermal hysteresis is more specifically defined as:

$$\Delta T = \frac{A_s + A_f}{2} - \frac{M_s + M_f}{2} \tag{2}$$

with the characteristic martensite temperatures assessed using the typical approach based on intersection of tangent lines as shown for A_s in **Fig. 3**.

Using the same conditions, an additional set of samples were prepared and subjected to thermal transformation cycles within the DSC. Between cycles, the samples were occasionally cooled to room temperature and transferred to the stereo microscope for characterization.

A. 1.5 mol% Y_2O_3 – ZrO_2

The strain-temperature curves generated by the TMA for the 1.5 mol% Y_2O_3 samples are displayed in **Fig. 4** with **a,b** corresponding to the single crystal and **c,d** corresponding to the polycrystal sample. Referring to the overlay of multiple transformation cycles for the single

crystal specimen (**Fig. 4a**), one can see that the cycles show good agreement in the transformation behavior, with the exception of the first transformation cycle; this difference is likely due to a "training" effect with some accumulation of dislocations (36), and perhaps a different degree of transformation attained under these cooling conditions as compared with the original solidification cooling during processing. **Fig. 4b** presents the evolution of the strain-temperature curve for a selection of cycles that include the 1st, the 5th to capture any early onset evolution, the 14th to capture any saturation effect, and the 45th or last cycle measured. It is clear that the single crystal transformation behavior appears stable with little variation in the height (strain % on heating) or width (thermal hysteresis) of the strain-temperature curves from cycle to cycle. The curve also appears to be a closed loop with no evidence of ratcheting or residual strain.

In stark contrast, the overlay plot for the polycrystal sample in **Fig. 4c** shows much less repeatability. There is a large spread in both the strains and thermal hysteresis. From **Fig. 4d**, it is clear that there is significant elongational ratcheting and residual strain accumulation in the early cycles, which diminishes on subsequent cycling until crossing over into a mode where ratcheting occurs in a shrinkage mode. The shrinkage mode is shown to persist and even increase in magnitude through the remaining tested cycles.

The parameters identified for analysis in **Fig. 3** are collected for these samples as a function of cycle number in **Fig. 5**, including thermal hysteresis (**Fig. 5a**), strain amplitude (**Fig. 5b**), and strain recovery (**Fig. 5c**), where positive values are elongational and negative values correspond to axial shrinkage. In general, the 1.5 mol% Y_2O_3 single crystal sample shows remarkable repeatability in terms of all analyzed parameters, indicating stability with cyclic martensitic transformation; the cycles are closed without residual strains and the hysteresis and strain amplitude are approximately constant at an average of 140 ℃ and 3.2%, respectively. Conversely, the polycrystal structure evolves through a decrease in thermal hysteresis until reaching a minimum of 167 ℃ on the 3rd cycle (**Fig. 5a**), followed by an increase to a maximum of 315 ℃ after 45 transformation cycles. The rate of change of hysteresis is quite high at first (from cycles 3 to 8, at ~15.4 ℃ per cycle) and then reduces. In **Fig. 5b**, the strain amplitude of the polycrystal first increases over the first three cycles, and then decreases until a fairly stable value of ~1.5% is reached at the 10th cycle. The polycrystal structure first shows significant net

positive residual strain (**Fig. 5c**), reaching a maximum on the 3rd cycle, and then dropping to negative values. The strain recovery continues to decrease in a steadier fashion beyond cycle 10.

The consistency of the single crystal cycle properties and the lack thereof in the polycrystal speak to a difference in the stability of those samples. These stability trends are strikingly confirmed in the photographs of **Fig. 6**, taken intermittently between thermal cycles in the DSC. For a given cycle, the polycrystal exhibits deterioration by intergranular cracking and subsequent grain loss while the single crystal does not. Mass loss measurements (**Fig. 5d**) confirm that small portions of the polycrystal are bodily lost from the bulk of the specimen upon cycling (and handling). At the final collected cycle (45th cycle), the polycrystal pellet is only 64.3% of its initial mass. The single crystal shows no discernable mass loss, even when cycled well past the last cycle measured for the polycrystal structure (45th), out to at least 125 cycles (**Fig. 6**).

The occurrence of cracking with thermal cycling of the polycrystalline sample provides a basis for interpretation of the curves in **Fig. 5a-c**. For example, all of the measured parameters appear to have a critical minimum or maximum on the 3rd cycle. These extrema suggest that in the first few cycles, there is crack initiation and associated swelling of the sample's extensive volume increase, as evidenced by the increase in strain amplitude (**Fig. 5b**) and residual strain (**Fig. 5c**). With subsequent cycling the sample integrity is further reduced prior to the onset of substantial mass loss, with a network of cracks permeating the sample along grain boundaries and triple junctions. The gradual disaggregation of the sample into a granular packing leads to the observed sign change of strain recovery (**Fig. 5c**), the increase in thermal hysteresis (**Fig. 5a**), and the decrease in strain amplitude (**Fig. 5b**), all of which are indicative of irreversible damage and energy losses as a result of the cyclic martensitic transformation. Finally, mass loss from grain drop-out sets on after the sample has achieved relatively stable cycling properties as a loose assemblage of individual small grains/crystals. This loose assemblage ratchets compressively on every cycle because it lacks sufficient cohesive restoring force.

B. 2.0 mol% Y_2O_3 – ZrO_2

The same basic set of cycling experiments was conducted on the 2.0 mol% Y_2O_3 samples as on the 1.5 mol% Y_2O_3 specimens, with the only difference being the lower transformation temperatures for 2.0 mol% Y_2O_3. The results of those experiments are largely the same as we

have just elaborated for the 1.5 mol% Y_2O_3 specimen with regards to the microstructural dependence of the transformation properties. Therefore, we only briefly present those results here, with TMA curves in **Fig. 7** and summarized cycling results in **Fig. 8**. After a training period in the first four cycles, the single crystal structure showed stable cycling, especially in comparison to the polycrystal structure, which shows significant variability in terms of hysteresis, forward strain amplitude, and level of residual strain with repeated transformations. This is confirmed to be due to the polycrystal's continually evolving microstructure with intergranular cracking, visually confirmed via stereo microscopy in **Fig. 6**.

With regards to the compositional dependence of the transformation behavior, **Figs. 5** and **8** can be directly compared. Close inspection finds that most of the measured variables in those figures show similar trends and magnitudes between the two compositions. The one exception to this is that the two single crystal samples exhibited a noticeable difference in their measured stable forward strain amplitudes, being about 0.9% for the 2.0 mol% Y_2O_3 samples and a much larger 3.2% for the 1.5 mol% Y_2O_3 sample (averaged from cycle 5 to the last collected cycle). We believe that this difference is likely due to the strong orientation dependence of the transformation strain; our measurement axis was selected without cognizance of the crystal orientation, and different orientations can easily show strain differences as large or even much larger than that found here (23). Interestingly, there is no clear composition dependence in the forward strain amplitude of the polycrystal specimen, which sample many orientations and thus are free of this effect.

As the compositions explored in this work are both within the shape memory regime, the similarities between the relative trends observed in the transformation behavior between the single crystal and polycrystal structures point to the impact of microstructure on martensitic transformation irrespective of the composition within this particular regime.

Discussion

The most prominent result of the present work is the observation that large mm-scale single crystals of zirconia survive the martensitic transformation, even through 125 cycles, and without measurable signatures of degradation in the thermal or strain response. This is significant since

polycrystalline zirconia compositions are widely known to fracture during the transformation, and the side-by-side comparison at the same composition in this work confirms a critical role of grain structure in such fracture. Prior studies on very small, micro-scale specimens of zirconia have shown cyclic transformation survivability of single crystals at the few-micron scale (11,18); this work extends the observation by about three orders of magnitude in length scale.

This observation also further builds the analogy of SMCs with their intermetallic counterparts, many of which exhibit cracking under cyclic martensitic transformations, especially in the Cu-based systems (12,13,16). In those systems the removal of grain boundaries and triple junctions has been related to lower internal mismatch stresses (14), which is certainly relevant in bulk single crystal SMCs as well. Moreover, the highly repeatable transformations in the present single crystals are accompanied by a very high uniaxial strain output of ~3.2%. To our knowledge this strain is the highest recorded without fracture for bulk ceramic zirconia; Tiefenbach et al. (37) reported less than 1% with apparent cracking in bulk 9 mol% CeO_2-ZrO, while Reyes-Morel et al. (4) demonstrated strain recovery of just 0.7% by the shape memory effect in 12 mol% CeO_2-ZrO_2.

We can further explore the SMC/SMA analogy through consideration of hysteresis, as in SMAs there is a well-established correlation between smaller hysteresis levels and better cyclic stability (38–43). For those metallic systems, polycrystal structures have a larger hysteresis than single crystal structures (44,45), but we are not aware that those trends have been previously established in martensitic ceramics. Our observations in **Figs. 5a** and **8a** align with the SMA literature in that the single crystals indeed have a lower hysteresis over most every cycle, in some cases by quite a large margin. We can also examine hysteresis in terms of the heat loss over a given full (two transformation) thermal cycle, which we explore in **Fig. 9a,b**. Here we show the evolution of the total heat absorbed on the reverse endothermic reaction (heat of austenite transformation Q_A) and released on the forward exothermic reaction (heat of martensite transformation Q_M), respectively, as measured in the DSC during cycling of the 1.5 mol% Y_2O_3 samples.

The heats of transformation for the single crystal structure, while more stable compared to those of the polycrystal structure, do show a small and gradual decrease with the number of transformation cycles, which we attribute to substructure evolution through generation and

motion of dislocations (36,46). By contrast, the polycrystal sample shows greater evolution of these heats over cycling, and greater variability between the forward and reverse transformations. In the forward transformation regime, the polycrystal deviates from the single crystal by releasing significantly more exothermic heat over the whole range of the cycling, with the most occurring in the first ~15 cycles. The reverse transformation seems to absorb the same amount of endothermic heat as does the single crystal, until approximately cycle 30, beyond which there is divergence.

When put together, the differences in these DSC signals between the polycrystal and single crystal speak to how energy is dissipated during the phase transformation; the samples have the same compositions and thus the same phase properties (such as heat capacity), and so the differences between them can be taken to reveal the effect of microstructure. In **Fig. 9c**, we show the net endothermic heat absorption after each full cycle of forward and reverse transformations (Q_A-Q_M); this quantity is positive because of the hysteresis of the transformation, which involves heat dissipation. We plot this energy normalized by the average value of the absolute heat released and absorbed over a cycle, $Q_{avg.} = \frac{1}{2}(Q_A+Q_M)$, to permit direct comparison between the two samples, and the y-axis thus plots the fraction of the transformation heat that is lost on each cycle. This quantity is relatively stable for the single crystal sample, which aligns with all of our prior observations above that the martensitic transformation is very repeatable with only limited structural evolution. However, in the polycrystal structure, this quantity is evolving continuously with cycling and is shifted in an exothermic direction as compared to the single crystal.

We believe that the difference between the curves in **Fig. 9c** is directly related to the additional mechanisms of structural evolution in the polycrystal, namely, cracking in the early cycles, followed perhaps by interparticle sliding and friction as the sample comminutes. Interestingly, the difference between the curves in **Fig. 9c** is large at first, but reduces on cycling as the polycrystal becomes a loose aggregate of small, presumably single crystalline particles; after about the 34th cycle, the powdered polycrystal has converged on the single crystal result to within some scatter.

Pursuing this line of reasoning, the difference between the polycrystal and single crystal trends in **Fig. 9c**, which is shaded and labeled E_{crack}, can be used to quantify the energy spent on cracking

in the polycrystal. By multiplying this difference by $Q_{avg.}$ of the polycrystal sample, the extra exothermic energy with cracking accumulated over each cycle ($E_{crack\ total}$) is presented in **Fig. 9d**.

According to our construction, **Fig. 9d** shows the total energy liberated by the sequence of cracking and comminution events over the course of thermal cycling. It is interesting that the rate of energy accumulation here is rapid at first, slowing gradually and then reaching an apparent plateau at about 10 kJ/mol around cycle 34. The shape of this trend is certainly consistent with the gradual cracking of the polycrystal over many cycles and its eventual disaggregation to a point where it need no longer crack. To evaluate whether the amount of released energy at ~10 kJ/mol is in line with expectations for cracking, we consider the classical Griffith-like view of brittle fracture as comprising an endothermic energy associated with surface creation ($E_{surface}$), and an exothermic contribution of stress relief attained by cracking ($E_{stress\ relief}$):

$$E_{cracking} = E_{stress\ relief} - E_{surface} \tag{3}$$

written such that positive values are exothermic (as in **Fig. 9c,d**).

The energy due to the creation of surfaces can be computed using a space-filling polyhedron (tetrakaidecahedra) to model the total grain boundary area A_{gb} and presuming that it cracks to give double that area in free surfaces with γ is the surface energy (given as 2.5 J/m^2 by Ref. (47)). For our grain size of ~1.0 μm, calculated from SEM (**Fig. 1a**), the predicted total surface energy is approximately 0.33 kJ/mol. The energy due to stress relief can be approximated using the total transformation strain energy density, $E_{stress\ relief} \sim \frac{1}{2} C_{ijkl}\varepsilon_{ij}\varepsilon_{kl}$, , with C_{ijkl} the fourth order stiffness tensor and ε_{ij} and ε_{kl} both represent the transformation strain tensor, which is computed from the stretch tensor minus the identity matrix. This calculation is an upper bound, as it assumes the full transformation takes place and is accommodated only elastically, but it should give a reasonable order of magnitude estimate. The inputs for this computation are given by Ref. (48) and (49), and yield a value of $E_{stress\ relief}$ = 15.3 kJ/mol.

We observe that the elastic relaxation energy is far larger than that of surface area creation (0.33 kJ/mol), so using Eq. 3, we expect a net exothermic cracking energy of about 15 kJ/mol. This value is of the same order of magnitude as the experimentally derived cracking energy accumulated over the course of cycling in **Fig. 9**, which amounts to about 10 kJ/mol. As expected, due to the upper-bound nature of our calculation of Eq. 3, the experimental value is

lower than the theoretical one. In light of this, the agreement is considered quite good, and we conclude, therefore, that the differences in the DSC data of our single crystal vs. polycrystalline samples are well explained in a quantitative sense by cracking.

Summary and Conclusions

We have studied cyclic martensitic transformation between monoclinic and tetragonal phases in single crystal and polycrystal zirconia-based SMCs in order to reveal the impact of grain boundaries on damage evolution. For two different compositions, thermal cycling experiments carried out over dozens of cycles revealed that single crystals had highly repeatable transformation behavior in terms of thermal hysteresis, strain amplitude, residual strain, and structural integrity, thereby encouraging further study of cold-crucible induction melting as a means to achieve SMCs with highly consistent transformation properties. In contrast, irreversible damage develops in the polycrystal sample beginning from the early cycles, where an increased strain amplitude and residual ratcheting strains point to an increase in volume associated with crack formation. Subsequent cycling led to the disaggregation of the pellet and was accompanied by an increase in hysteresis, decrease in strain amplitude, and sign change in the residual strain. The development of cracks also had a measurable influence on energy dissipation, which we examined by assessing the difference in the transformation enthalpies on the forward and reverse transformations, and comparing the single crystal and polycrystal samples quantitatively. The evolution of cracks could explain an extra exothermic quantity of energy on each cycle of the polycrystal, until it was fully disaggregated after about 35 cycles.

The suppression of cracking that we see in single crystals of ZrO_2 compositions during the monoclinic-tetragonal transformation aligns with observations in the literature but at a much larger length scales: reducing grain boundaries and triple junctions lowers internal stress concentrations and helps avoid intergranular fracture. Whereas most prior studies of this effect are in micron-scale samples, this work, by fabricating larger scale single crystals, brings the discussion of shape memory properties in zirconia into the millimeter range and presents cold-crucible induction melting as a potentially viable method for the production of SMCs. Future investigations should examine cyclic transformation triggered under stress (superelastic cycles), and be compared to the present thermal transformations in the shape memory regime.

Acknowledgements

References

1. Chevalier J, Gremillard L, Virkar AV, Clarke DR. The tetragonal-monoclinic transformation in zirconia: Lessons learned and future trends. J Am Ceram Soc. 2009 Sep;92(9):1901–20.

2. Hannink RHJ, Kelly PM, Muddle BC. Transformation toughening in zirconia-containing ceramics. J Am Ceram Soc. 2004 Dec 21;83(3):461–87.

3. Subbarao EC, Maiti HS, Srivastava KK. Martensitic transformation in zirconia. Phys Status Solidi. 1974 Jan 16;21(1):9–40.

4. Reyes-Morel PE, Jyh-Shiarn C, Chen I-W. Transformation plasticity of CeO2-stabilized tetragonal zirconia polycrystals: II, Pseudoelasticity and shape memory effect. J Am Ceram Soc. 1988 Aug 1;71(8):648–57.

5. Garvie RC, Hannink RHJ, Pascoe RT. Ceramic steel? Nature. 1975 Dec 25;258(5537):703–4.

6. Gupta TK, Bechtold JH, Kuznicki RC, Cadoff LH, Rossing BR. Stabilization of tetragonal phase in polycrystalline zirconia. J Mater Sci. 1977 Dec;12(12):2421–6.

7. Zeng XM, Du Z, Schuh CA, Tamura N, Gan CL. Microstructure, crystallization and shape memory behavior of titania and yttria co-doped zirconia. J Eur Ceram Soc. 2016 Apr 1;36(5):1277–83.

8. Camposilvan E, Torrents O, Anglada M. Small-scale mechanical behavior of zirconia. Acta Mater. 2014 Nov 1;80:239–49.

9. Camposilvan E, Anglada M. Size and plasticity effects in zirconia micropillars compression. Acta Mater. 2016 Jan 15;103:882–92.

10. Chen I-W, Xue LA. Development of superplastic structural ceramics. J Am Ceram Soc. 1990 Sep 1;73(9):2585–609.

11. Lai A, Du Z, Gan CL, Schuh CA. Shape memory and superelastic ceramics at small scales.

Science. 2013;341(6153):1505–8.

12. Bertolino G, Larochette PA, Castrodeza EM, Mapelli C, Baruj A, Troiani HE. Mechanical properties of martensitic Cu–Zn–Al foams in the pseudoelastic regime. Mater Lett. 2010 Jul 15;64(13):1448–50.

13. Oshima R, Yoshida N. Fatigue of thermoelastic Cu-Zn-Al alloys. Le J Phys Colloq. 1982 Dec 1;43(C4):803–8.

14. Ueland SM, Schuh CA. Grain boundary and triple junction constraints during martensitic transformation in shape memory alloys. J Appl Phys. 2013 Aug 7;114(5):053503.

15. Chen Y, Zhang X, Dunand DC, Schuh CA. Shape memory and superelasticity in polycrystalline Cu-Al-Ni microwires. Appl Phys Lett. 2009;95(17):171906.

16. Ueland SM, Schuh CA. Superelasticity and fatigue in oligocrystalline shape memory alloy microwires. Acta Mater. 2012 Jan 1;60(1):282–92.

17. Du Z, Zeng XM, Liu Q, Lai A, Amini S, Miserez A, et al. Size effects and shape memory properties in ZrO2 ceramic micro- and nano-pillars. Scr Mater. 2015 May 1;101:40–3.

18. Du Z, Zeng XM, Liu Q, Schuh CA, Gan CL. Superelasticity in micro-scale shape memory ceramic particles. Acta Mater. 2017 Jan 15;123:255–63.

19. Du Z, Ye P, Zeng XM, Schuh CA, Tamura N, Zhou X, et al. Synthesis of monodisperse CeO2 - ZrO2 particles exhibiting cyclic superelasticity over hundreds of cycles. J Am Ceram Soc. 2017 Sep;100(9):4199–208.

20. Zhao X, Lai A, Schuh CA. Shape memory zirconia foams through ice templating. Scr Mater. 2017 Jul 1;135:50–3.

21. Yu HZ, Hassani-Gangaraj M, Du Z, Gan CL, Schuh CA. Granular shape memory ceramic packings. Acta Mater. 2017 Jun 15;132:455–66.

22. Rauch HA, Chen Y, An K, Yu HZ. In situ investigation of stress-induced martensitic transformation in granular shape memory ceramic packings. Acta Mater. 2019 Apr 15;168:362–75.

23. Zeng XM, Lai A, Gan CL, Schuh CA. Crystal orientation dependence of the stress-induced martensitic transformation in zirconia-based shape memory ceramics. Acta Mater. 2016 Sep 1;116:124–35.

24.   Kuz′minov I, Lomonova E, Osiko V. Cubic zirconia and skull melting. Cambridge International Science Publishing Ltd; 2008. 346 p.

25.   Xu J, Lei X, Jiang X, He Q, Fang Y, Zhang D, et al. Industrial growth of yttria-stabilized cubic zirconia crystals by skull melting process. J Rare Earths. 2009 Dec 1;27(6):971–4.

26.   Osiko VV., Borik MA, Lomonova EE. Synthesis of refractory materials by skull melting technique. In: Dhanaraj G, Byrappa K, Prasad V, Dudley M (eds) Springer Handbook of Crystal Growth Springer Handbooks. Springer, Berlin, Heidelberg; 2010. p. 433–77.

27.   Prettyman KM, Jue JF, Virkar AV., Hubbard CR, Cavin OB, Ferber MK. Hysteresity effects in 3 mol% yttria-doped zirconia (t'-phase). J Mater Sci. 1992 Aug;27(15):4167–74.

28.   Toraya H, Yoshimura M, Somiya S. Calibration curve for quantitative analysis of the monoclinic-tetragonal ZrO2 system by x-ray diffraction. J Am Ceram Soc. 1984 Jun;67(6):C-119-C–121.

29.   Gauna MR, Conconi MS, Gomez S, Suárez G, Aglietti EF, Rendtorff NM. Monoclinic-tetragonal zirconia quantification of commercial nanopower mixtures by XRD and DTA. Ceramics-Silikáty. 2015;59(4):318–25.

30.   Hajizadeh-Oghaz M, Razavi RS, Estarki ML. Large-scale synthesis of YSZ nanopowder by Pechini method. Bull Mater Sci. 2014;37(5):969–73.

31.   Quinelato AL, Longo E, Leite ER, Bernardi MIB, Varela JA. Synthesis and sintering of ZrO2-CeO2 powder by use of polymeric precursor based on Pechini process. J Mater Sci. 2001;36(15):3825–30.

32.   Sunde TOL, Grande T, Einarsrud M-A. Modified Pechini Synthesis of Oxide Powders and Thin Films. In: Klein L, Aparicio M, Jitianu A (eds) Handbook of Sol-Gel Science and Technology. Springer, Cham; 2016. p. 1–30.

33.   Ruh R, Mazdiyasni KS, Valentine PG, Bielstein HO. Phase Relations in the System ZrO2-Y2O3 at Low Y2O3 Contents. Commun Am Ceram Soc. 1984;67(9):190–2.

34.   Patil RN, Subbarao EC. Axial thermal expansion of ZrO2 and HfO2 in the range room temperature to 1400°C. J Appl Crystallogr. 1969 Dec 1;2(6):281–8.

35.   Geller RF, Yavorsky PJ. Effects of some oxide additions on the thermal length changes of zirconia. J Res Natl Bur Stand (1934). 1945 Jul;35(1):87.

36.   Maletta C, Sgambitterra E, Furgiuele F, Casati R, Tuissi A. Fatigue properties of a pseudoelastic

NiTi alloy: Strain ratcheting and hysteresis under cyclic tensile loading. Int J Fatigue. 2014 Sep 1;66:78–85.

37.   Tiefenbach A, Wagner S, Oberacker R, Hoffmann B. Measurement of the t→m and m→t transformations in Ce–TZP by dilatometry and impedance spectroscopy. J Eur Ceram Soc. 2002 Mar 1;22(3):337–45.

38.   Ōtsuka K, Wayman CM. Shape memory materials. Cambridge University Press; 1998.

39.   Gall K, Maier H. Cyclic deformation mechanisms in precipitated NiTi shape memory alloys. Acta Mater. 2002 Oct;50(18):4643–57.

40.   Grossmann C, Frenzel J, Sampath V, Depka T, Eggeler G. Elementary transformation and deformation processes and the cyclic stability of NiTi and NiTiCu shape memory spring actuators. Metall Mater Trans A. 2009 Nov 21;40(11):2530–44.

41.   Atli KC, Franco BE, Karaman I, Gaydosh D, Noebe RD. Influence of crystallographic compatibility on residual strain of TiNi based shape memory alloys during thermo-mechanical cycling. Mater Sci Eng A. 2013 Jul 1;574:9–16.

42.   Kato H, Ozu T, Hashimoto S, Miura S. Cyclic stress–strain response of superelastic Cu–Al–Mn alloy single crystals. Mater Sci Eng A. 1999 May;264(1–2):245–53.

43.   Song Y, Chen X, Dabade V, Shield TW, James RD. Enhanced reversibility and unusual microstructure of a phase-transforming material. Nature. 2013;502(7469):85–8.

44.   Hautcoeur A, Fouché F, Sicre J. Cu-Al-Ni shape memory single crystal wires with high transformation temperature. In: Proceedings of the 43rd Aerospace Mechanisms Symposium. NASA Ames Research Center; 2016. p. 185–91.

45.   Hamilton R., Sehitoglu H, Chumlyakov Y, Maier H. Stress dependence of the hysteresis in single crystal NiTi alloys. Acta Mater. 2004 Jun 21;52(11):3383–402.

46.   Morgan NB, Friend CM. A review of shape memory stability in NiTi alloys. Le J Phys IV. 2001 Nov;11(PR8):325–32.

47.   Christensen A, Carter EA. First-principles study of the surfaces of zirconia. Phys Rev B. 1998 Sep 15;58(12):8050–64.

48.   Chan S-K, Fang Y, Grimsditch M, Li Z, Nevitt MV., Robertson WM, et al. Temperature dependence of the elastic moduli of monoclinic zirconia. J Am Ceram Soc. 1991 Jul

1;74(7):1742–4.

49.   Simha N. Twin and habit plane microstructures due to the tetragonal to monoclinic transformation of zirconia. J Mech Phys Solids. 1997 Feb;45(2):261–3.

Table 1. The measured critical transformation temperatures for the as-prepared polycrystal and single crystal specimens.

Composition	Single Crystal (℃)				Polycrystal (℃)			
	M_s	M_f	A_s	A_f	M_s	M_f	A_s	A_f
1.5 mol% Y_2O_3	643	478	594	743	551	504	671	709
2.0 mol% Y_2O_3	500	322	476	603	412	316	499	618

Fig. 1. Single crystals used in the present work; (a-c) correspond to 1.5 mol% Y_2O_3 crystal, and (d-f) correspond to 2.0 mol% Y_2O_3 crystal. (a,d) stereo microscopy images, (b,e) integrated 1D X-ray diffraction spectra with labeled characteristic tetragonal (t) and monoclinic (m) peaks and inset of the 2D pattern, and (c,f) differential scanning calorimeter curves with labeled critical transformation temperatures.

Fig. 2. Polycrystal specimens used in the present work; (a-c) correspond to 1.5 mol% Y_2O_3 crystal, and (d-f) correspond to 2.0 mol% Y_2O_3 crystal. (a,d) scanning electron microscopy showing the grain structure of the sintered pellets, (b,e) in-situ XRD for a complete transformation cycle with labeled critical transformation temperatures, and (c,f) differential scanning calorimeter thermal curves with labeled critical transformation temperatures.

Fig. 3. A single characteristic strain-temperature hysteresis loop for the 1.5 mol% Y_2O_3 polycrystal

specimen with labeled key components including (a) negative residual strain, (b) strain amplitude of reverse transformation on heating, and (c) thermal hysteresis with labeled critical transformation temperatures.

Fig. 4. Transformation hysteresis loops in strain-temperature space for the 1.5 mol% Y_2O_3 single crystal and polycrystal structures; (a-b) correspond to curves generated for the single crystal specimen while (c-d) correspond to polycrystal equivalent. (a,c) overlaid hysteresis loops for transformation cycles and (b,d) select cycles plotted adjacent to one another.

Fig. 5. Extracted thermal cycling characteristics in 1.5 mol% Y_2O_3 single crystal and polycrystal structures as a function of the thermal cycle number N; (a) thermal hysteresis, (b) strain amplitude, (c) residual strain between final and initial strain measurements on each cycle, and (d) nominal mass. (a-c) were parameters extracted from TMA thermal hysteresis curves and (d) was measured using the DSC.

Fig. 6. Stereo microscopy images of (A) 1.5 mol% Y_2O_3 single crystal, (B) 1.5 mol% Y_2O_3 polycrystal structures, and (C) 2.0 mol% Y_2O_3 polycrystal structure, collected in between thermal cycles conducted in the DSC. The cycle number is denoted in the upper left-hand corner of each image with the direction of increasing cycles indicated by the arrow.

Fig. 7. Transformation hysteresis loops in strain-temperature space for the 2.0 mol% Y_2O_3 single crystal and polycrystal structures; (a-b) correspond to curves generated for the single crystal specimen while (c-d) correspond to polycrystal equivalent. (a,c) overlaid hysteresis loops for transformation cycles and (b,d) select cycles plotted adjacent to one another.

Fig. 8. Extracted thermal cycling characteristics in 2.0 mol% Y_2O_3 single crystal and polycrystal structures as a function of the thermal cycle number N; (a) thermal hysteresis, (b) strain amplitude, and (c) residual strain between final and initial strain measurements on each cycle. (a-c) were parameters extracted from TMA thermal hysteresis curves.

Fig. 9. Calorimetry analysis of energy dissipation for 1.5 mol% Y_2O_3 samples; (a) total heat released on the reverse endothermic reaction, (b) total heat absorbed on the forward exothermic reaction, (c) fraction of net endothermic heat absorbed after each full cycle of forward and reverse transformations, (d) cumulative total cracking energy in the polycrystal, found by accumulating the extra exothermic energy found relative to the single crystal in (c).
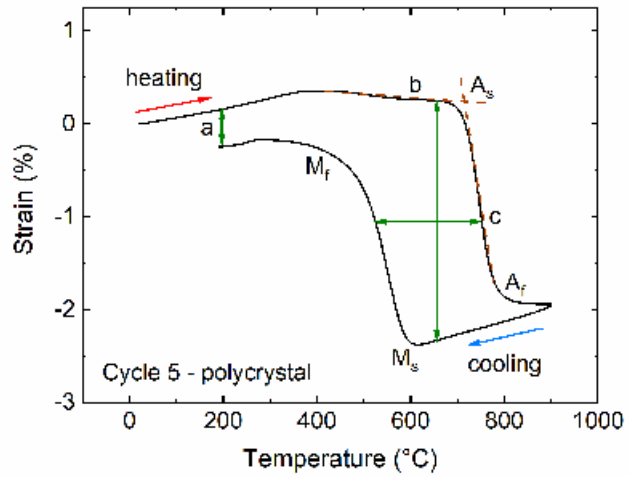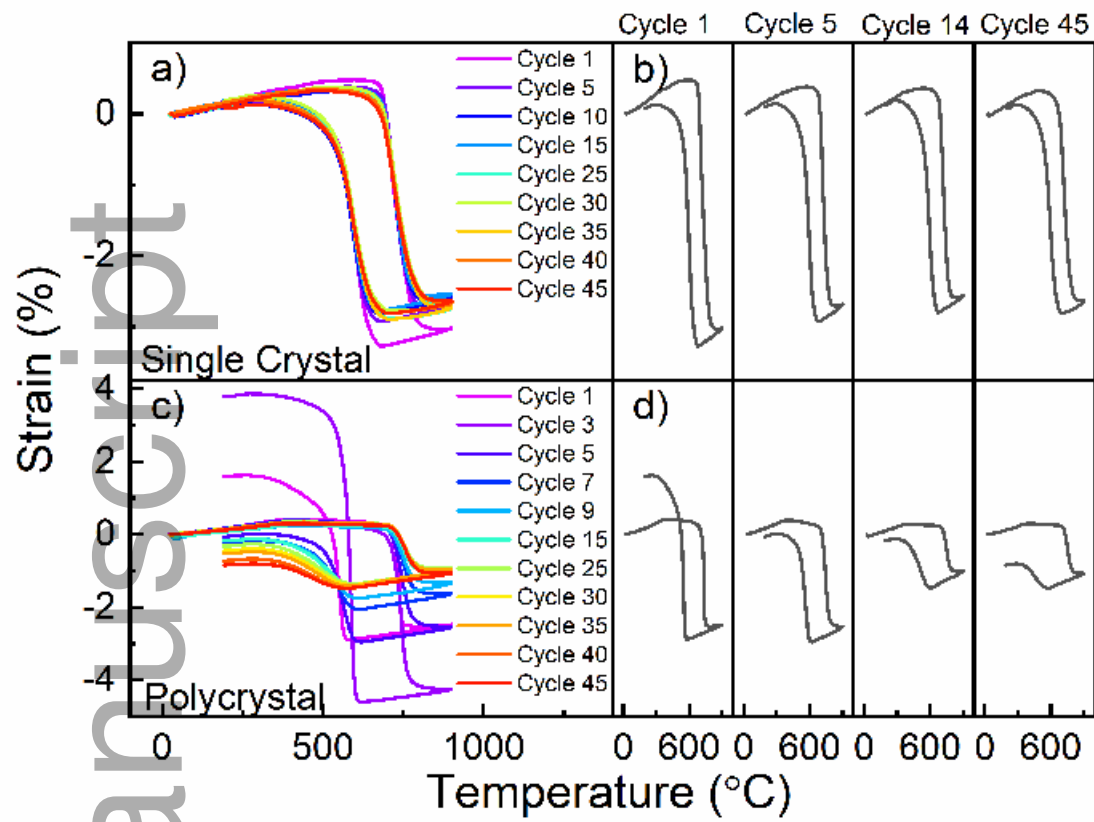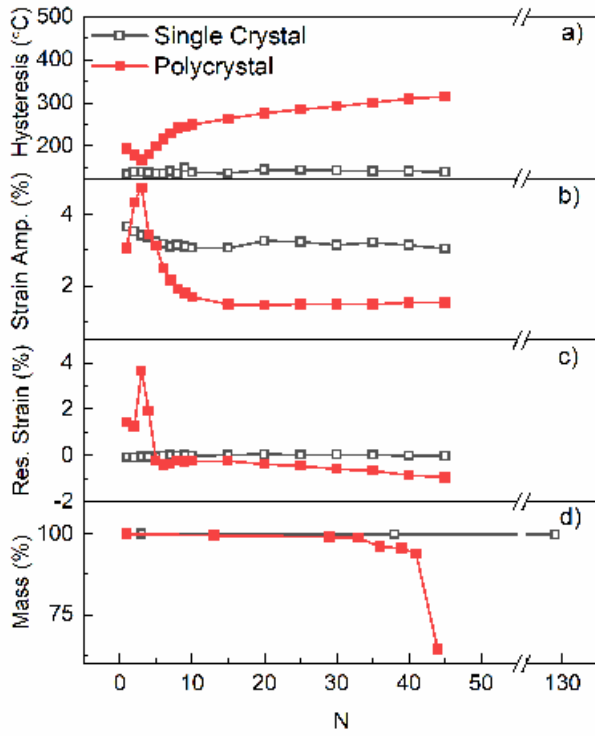
1.5 mol% Y_2O_3 2.0 mol% Y_2O_3

jace_17117_f1.tif
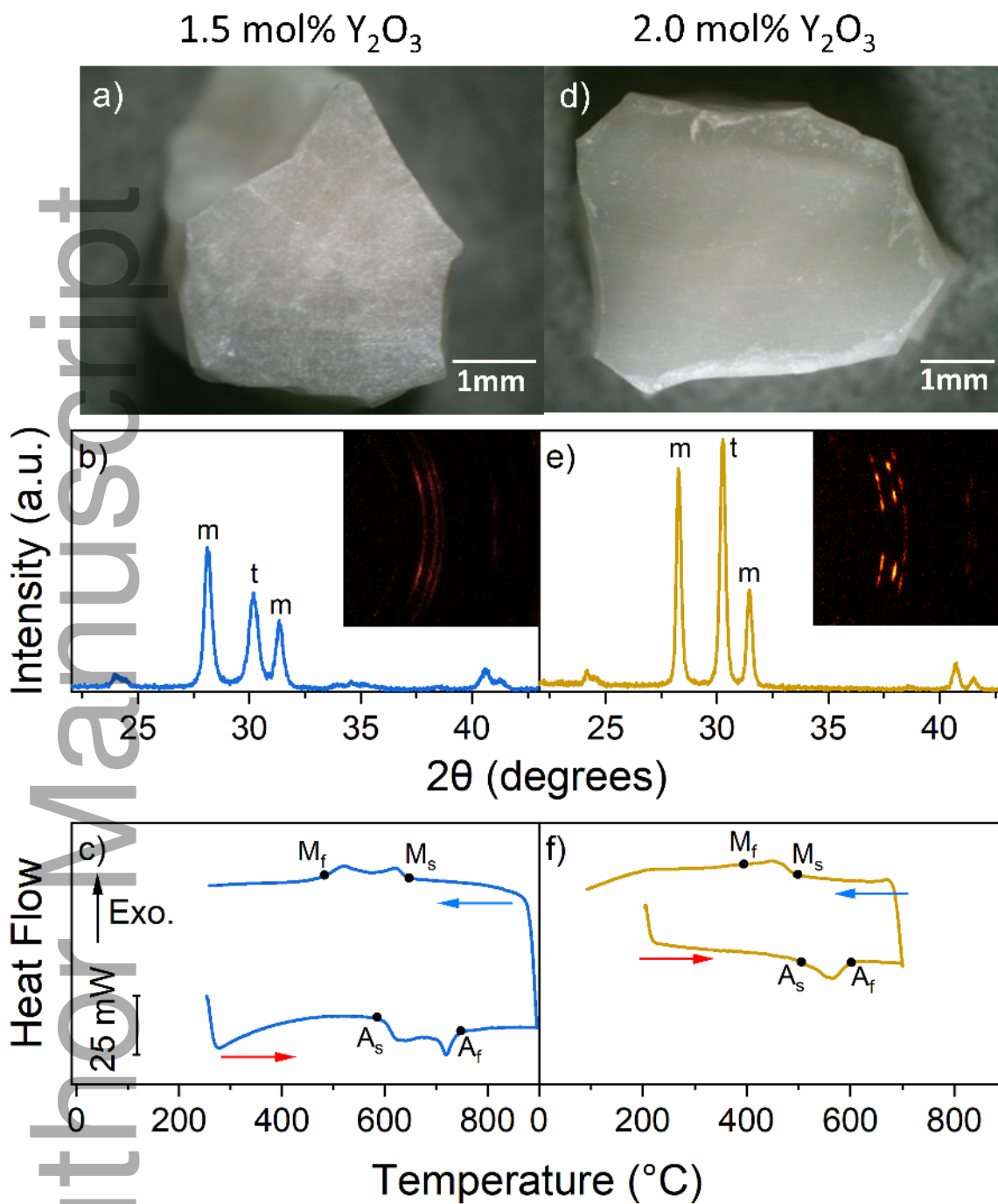
1.5 mol% Y₂O₃ — 2.0 mol% Y₂O₃
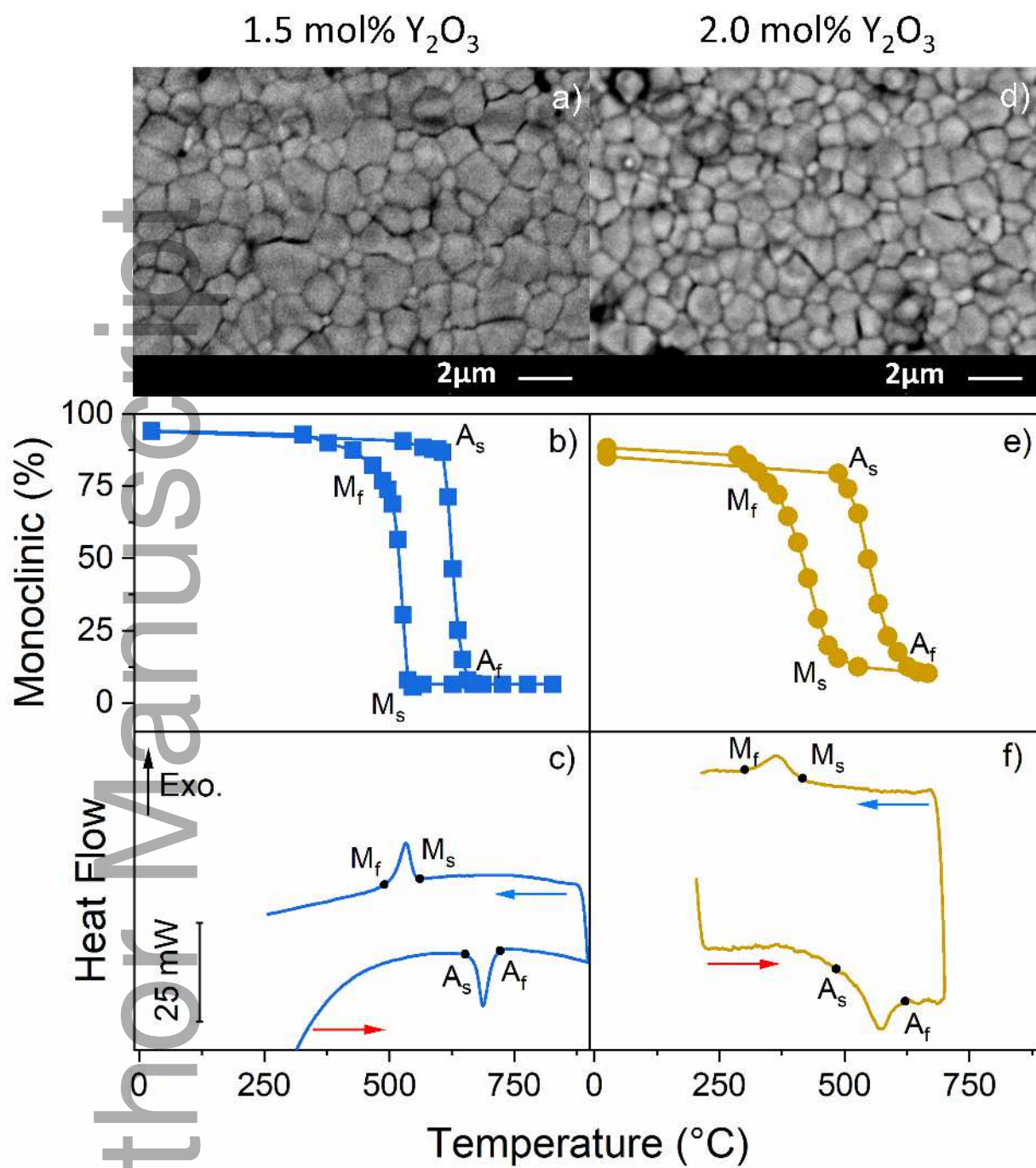
jace_17117_f2.tif

jace_17117_f3.tif

jace_17117_f4.tif

jace_17117_f5.tif

Thermal cycles

A. Single Crystal (1.5 mol% Y_2O_3)
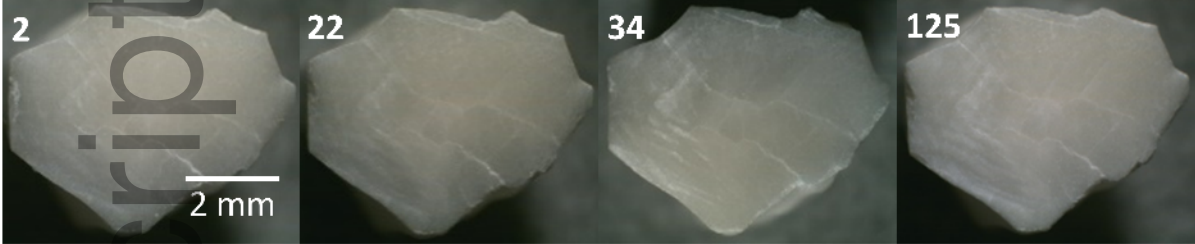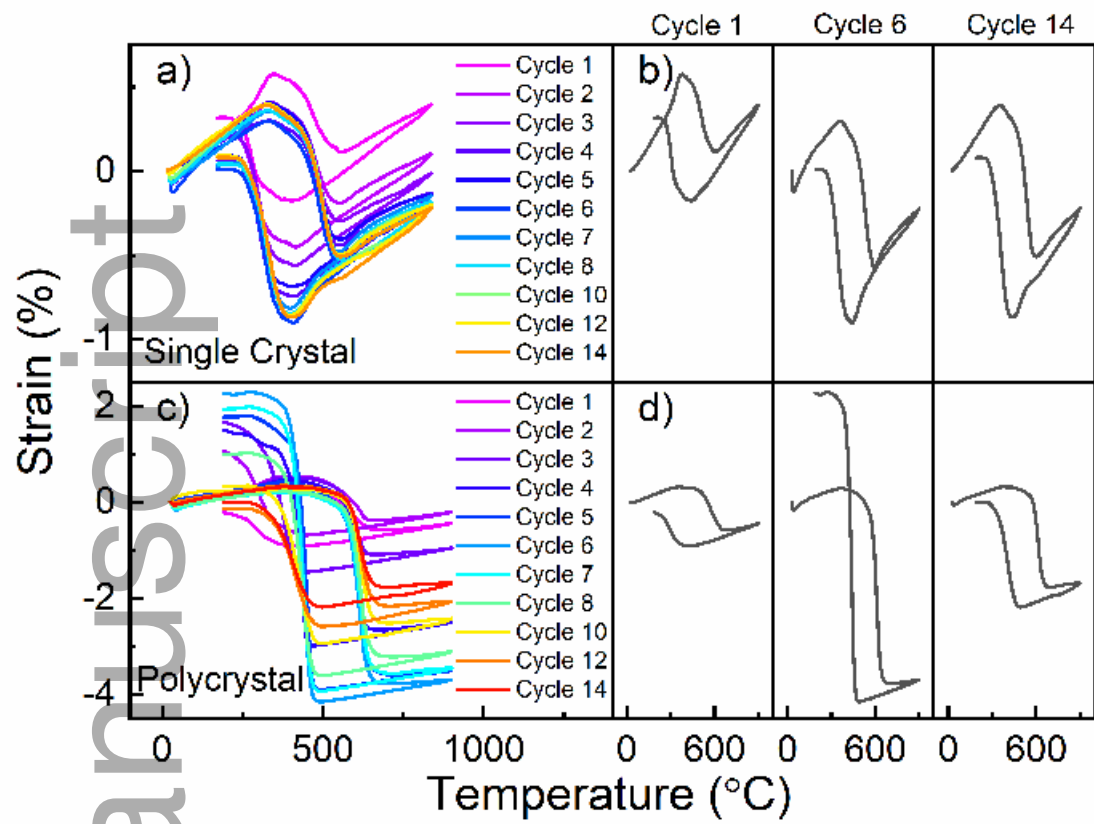
B. Polycrystal (1.5 mol% Y_2O_3)
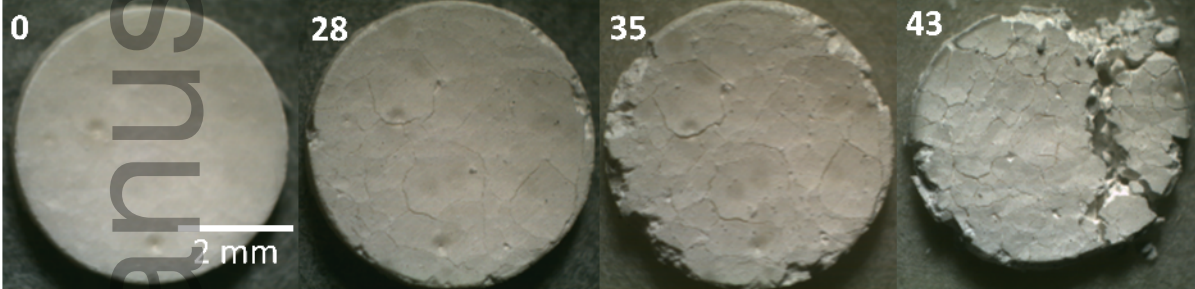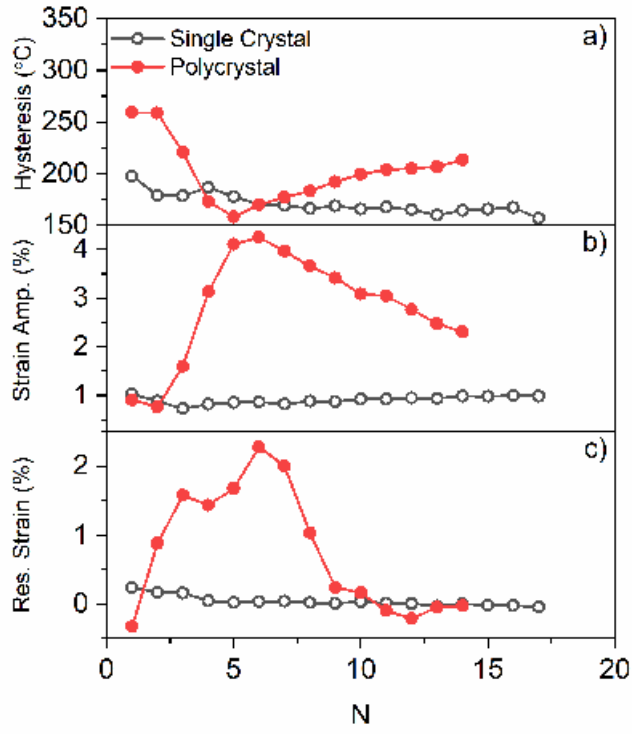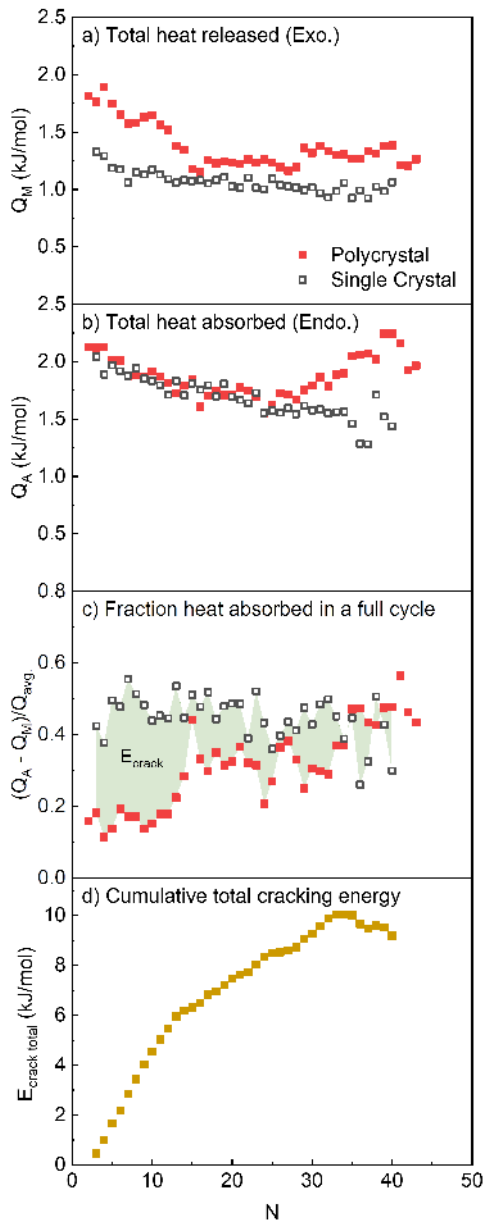
C. Polycrystal (2.0 mol% Y_2O_3)
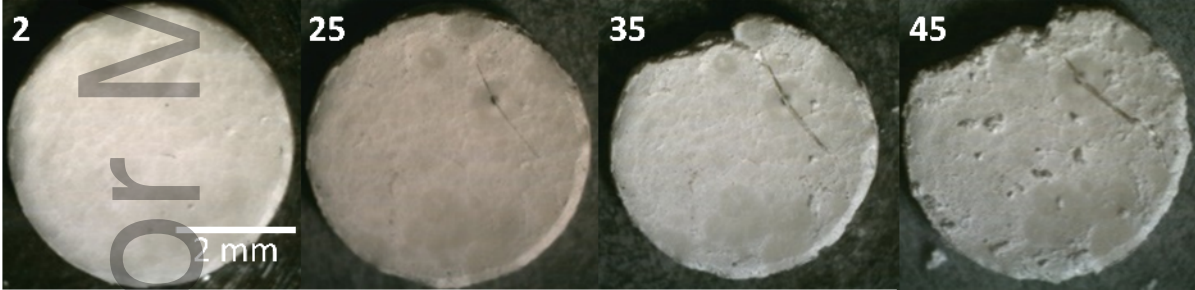
jace_17117_f6.tif

jace_17117_f7.tif

jace_17117_f8.tif

jace_17117_f9.tif